



Journal of Geophysical Research: Atmospheres

RESEARCH ARTICLE

10.1029/2018JD028369

Special Section:

Water-soil-air-plant-human nexus: Modeling and observing complex land-surface systems at river basin scale

Key Points:

- A high-resolution land surface model including groundwater lateral flow, water use, and soil freeze-thaw front dynamics was developed
- Simulations for Heihe River Basin in China showed that the active layer thickness increased over the permafrost zone
- Water use raised the latent heat flux and reduced the sensible heat flux, net ecosystem exchange, and streamflow recharging to an eco-fragile region

Correspondence to:

Z. Xie,
zxie@lasg.iap.ac.cn

Citation:

Xie, Z., Liu, S., Zeng, Y., Gao, J., Qin, P., Jia, B., et al. (2018). A high-resolution land model with groundwater lateral flow, water use, and soil freeze-thaw front dynamics and its applications in an endorheic basin. *Journal of Geophysical Research: Atmospheres*, 123. <https://doi.org/10.1029/2018JD028369>

Received 22 JAN 2018

Accepted 19 JUN 2018

Accepted article online 27 JUN 2018

A High-Resolution Land Model With Groundwater Lateral Flow, Water Use, and Soil Freeze-Thaw Front Dynamics and its Applications in an Endorheic Basin

Zhenghui Xie^{1,2} , Shuang Liu^{1,2} , Yujin Zeng^{1,3} , Junqiang Gao^{1,4}, Peihua Qin¹ , Binghao Jia¹ , Jinbo Xie¹ , Bin Liu^{1,2}, Ruichao Li^{1,2}, Yan Wang^{1,2}, and Longhuan Wang^{1,2}

¹State Key Laboratory of Numerical Modeling for Atmospheric Sciences and Geophysical Fluid Dynamics, Institute of Atmospheric Physics, Chinese Academy of Sciences, Beijing, China, ²College of Earth Science, University of Chinese Academy of Sciences, Beijing, China, ³Program in Atmospheric and Oceanic Sciences, Princeton University, Princeton, NJ, USA, ⁴School of Mathematics and Statistics, Nanjing University of Information Science and Technology, Nanjing, China

Abstract Human water regulation, groundwater lateral flow, and the movement of frost and thaw fronts (FTFs) affect soil water and thermal processes, as well as energy and water exchanges between the land surface and atmosphere. Reasonable representation of these processes in land surface models is very important to improving the understanding of land-atmosphere interactions. In this study, mathematical descriptions of groundwater lateral flow, human water regulation, and FTFs were synchronously incorporated into a high-resolution community land model, which is then named the Land Surface Model for Chinese Academy of Sciences (CAS-LSM). With a series of atmospheric forcings and high-resolution land surface data from the Heihe Watershed Allied Telemetry Experimental Research (HiWATER) program, numerical simulations of the period 1981–2013 using CAS-LSM with 1-km resolution were conducted for an endorheic basin, the Heihe River Basin in China. Compared with observations, CAS-LSM reproduced the distributions of groundwater, evapotranspiration, and permafrost reasonably and well matched the temporal changes in ground temperature, heat fluxes, and FTFs. Results illuminate the temporal and spatial characteristics of frozen soil and the changes in the land-atmosphere exchange of carbon, water, and energy. The permafrost and seasonally frozen soil were distinguished. In the seasonally frozen areas, the maximum soil frost depth increased by 0.65 mm/year within natural areas and decreased by 2.12 mm/year in human-dominated areas. The active layer thickness increased 8.63 mm/year for permafrost. In the permafrost zone evapotranspiration and latent heat flux increased, and the sensible heat flux declined. In the human-dominated areas water use raised the latent heat flux and reduced the sensible heat flux, net ecosystem exchange, and streamflow recharging to the eco-fragile region in the lower reaches. Results suggested that the land surface model CAS-LSM is a potential tool for studying land surface processes, especially in cold and arid regions experiencing human interventions.

1. Introduction

Interaction between human activities and water plays an important role in the eco-hydrological system (Pokhrel et al., 2016). The interaction is complicated by agricultural activities including water withdrawal and irrigation, which can significantly change the flow regimes of both surface water and groundwater (GW; Shah, 2014; Siebert et al., 2014). The magnitude of hydrological droughts has been intensified by human water use (Wada et al., 2013; Yuan et al., 2017), water abstractions have strongly affected water allocation and residence time (De Graaf et al., 2014), and anthropogenic GW exploitation has deepened the water table and rapidly reduced terrestrial water storage, while irrigation has increased soil moisture (Zeng, Xie, Yu, Liu, Wang, Zou, et al., 2016). Some studies show the importance of groundwater lateral flow (GLF; Fan, 2015; Ji et al., 2017; Maxwell & Condon, 2016; Xie et al., 2012; Zeng, Xie, Yu, Liu, Wang, Zou, et al., 2016). On the other hand, the status of frozen soil, as an indicator, reflects the impacts of both climate change and anthropogenic activities (Cheng & Wu, 2007; Li et al., 2008). The processes of soil freezing and thawing affect both soil moisture and temperature, the carbon-nitrogen (C-N) cycle, and water exchanges between the land surface and the atmosphere, as well as human activities such as engineering construction (Harada et al., 2009; Iwata et al., 2010; Pang et al., 2009; Schuur et al., 2009; Xia et al., 2017). The processes of soil frost and thaw, GLF, and human water use are closely impacted by the cycle

of water and energy. Understanding these complex processes and reasonably representing them in a land surface model is very important for global and regional water monitoring, environmental protection, and social development (Tian et al., 2016; Wood et al., 2011; Xie et al., 2016). As one crucial part of existing Earth system models, land models have provided an opportunity to study changes in water resources, ecological dynamics, and their interactions with climate (Lawrence et al., 2011).

Including a description of the GW in land surface models has experienced a long history of development (Fan, 2015; Liang & Xie, 2001, 2003; Niu et al., 2005; Zeng, Xie, Yu, Liu, Wang, Zou, et al., 2016). Liang and Xie (2003) accounted for groundwater table (GWT) dynamics in an explicit way in their land surface model. Zeng, Xie, Yu, Liu, Wang, Zou, et al. (2016) introduced a scheme of GLF into a community land model (CLM) and better reproduced the spatial pattern of GW depth at both river and basin scales. GW dynamics is often linked with human water regulation (HWR; Pokhrel et al., 2015; Xie et al., 2017; Yao et al., 2015; Zeng, Xie, & Liu, 2017; Zeng, Xie, & Zou, 2017). In addition, the changes in depth of frost and thaw fronts (FTFs) can be regarded as an important climatic and environmental indicator (Frauenfeld et al., 2004; Yi et al., 2006). Recently, Gao et al. (2016) incorporated the Stefan method for multilayered systems to simulate FTFs, which provided an important tool to diagnose the change in frozen soil and climate change.

However, current land surface models do not synchronously describe GLF, HWR, and the changes in FTFs and their interactions. In this study, descriptions of GLF, HWR, and the changes in FTFs were simultaneously incorporated into a CLM (CLM4.5) that contained representations of carbon and nitrogen processes and an active crop module. Then the integrated model was applied at the high spatial resolution of 1 km to the endorheic Heihe River Basin (HRB) in China. The objective of the study was to explore the temporal and spatial characteristics of frozen soil and the hydrological and ecological dynamics in both permafrost and human-dominated areas during the past 30 years.

2. Model Development

2.1. CLM4.5 and HWR

The CLM4.5 (Oleson, 2013) was used as the base model into which the three schemes of GLF, HWR, and FTFs were incorporated to produce a high-resolution model capable of simulating GLF, water use, and soil freeze-thaw front dynamics. CLM4.5 was developed by the National Center for Atmospheric Research, and it is the land surface component of the Community Earth System Model (CESM) 1.2.0 (Hurrell et al., 2013). The model CLM4.5 includes biogeophysical and biogeochemical mechanisms and energy and mass fluxes from the land to the atmosphere. Biogeochemical processes including vegetation photosynthesis, phenology, the carbon and nitrogen cycles, decomposition, and wildfires also are represented in CLM4.5 (Lindsay et al., 2014). CLM4.5 also contains an interactive crop management model, which simulates crop growth and its effects on land processes. CLM4.5 uses a subgrid hierarchy of land units, soil profiles, and plant function types to describe the heterogeneity within each grid cell. Different land uses, such as varieties of vegetation, lakes, urban areas, and glaciers, are addressed separately even if they coexist in a given grid cell.

A scheme of HWR was incorporated into CLM4.5 as a submodel (Zeng, Xie, & Liu, 2017; Zou et al., 2015). Water withdrawal is classified as GW pumping and surface water intake. GW pumping can be visualized as a process that extracts water from an aquifer. Correspondingly, surface water withdrawal can be described as a process that extracts water from rivers. Finally, according to actual water consumption data, the fractional extracted water is added on the topsoil layer in the model. The surface water withdrawal is written as

$$S' = S - q_s \Delta t, \quad (1)$$

where Δt is the time step of CLM4.5; S and S' denote the surface water storage before and after withdrawing water, respectively; and q_s is the rate of surface water use. The GW withdrawal is written as

$$W' = W - q_g \Delta t, \quad (2)$$

where W and W' are, respectively, the water storage in an aquifer before and after GW pumping and q_g is the rate of GW exploitation. After GW pumping, the GWT changes as

$$h' = h - \frac{q_g \times \Delta t}{s}, \quad (3)$$

where h and h' are, respectively, the simulated GW level before and after GW pumping and s is the aquifer-specific yield determined by CLM4.5. It should be noted that W and h in this module consider the impact of water use by hydrological processes in soil, such as water infiltration.

2.2. GLF

In the current work, based on the existing GW model for the vertical direction in CLM4.5, we used a two-dimensional GW movement equation to realize the GW exchange between grid cells. The GLF calculation is derived from Darcy's law and the Dupuit approximation (Bear, 1972) as:

$$R_l = \frac{\partial}{\partial x} \left(T \frac{\partial h}{\partial x} \right) + \frac{\partial}{\partial y} \left(T \frac{\partial h}{\partial y} \right), \quad (4)$$

where R_l is the GLF net discharge or recharge rate per unit area; x and y are the lengths in the longitude and latitude directions, respectively; T is the transmissivity; and h is the GWT head. Then the discretization of GLF for each grid cell in the simulation space is expressed as

$$R_{ij} = \sum_{n=1}^8 \frac{w_{ij} T_{ij} (h_n - h_{ij})}{S_{ij} l_n}, \quad (5)$$

where R_{ij} is GLF for the number of the i th row and the j th column of the model grid cell, n is the number of the eight neighboring grid cells, w_{ij} is the width of the flow cross section of the grid cell, h_{ij} is the GWT head of the grid cell, S_{ij} is the area of the grid cell, and l_n is the center-to-center distance between the grid cell and its neighbor.

The calculated lateral hydraulic conductivity of the surface soil at saturation was taken from Zeng, Xie, Yu, Liu, Wang, Zou, et al. (2016). After the lateral water exchange rate for each model grid cell was calculated, the water storage in the aquifer was written as

$$W'' = W + R \times \Delta t, \quad (6)$$

where W is the water storage in an aquifer before lateral water flow and R is the GLF for the time step Δt .

The simulated GW level h'' after lateral water flow can be written as follows:

$$h'' = h + \frac{R \times \Delta t}{s}, \quad (7)$$

where h is the simulated GW level before lateral water flow.

W and h in equations (6) and (7), respectively, can be closely linked with the impact of water use by the computations in equations (2) and (3), and hence, the interaction between HWR and GLF is represented in the model. When the GW is excessively exploited at some grid cell, the GW level will be lower than that in neighboring grid cells so that the GW in the neighboring cells will recharge the overexploited zone by GLF. This process would change the soil moisture, evaporation, and other related land surface variables, which are important for land-atmosphere coupling.

2.3. Soil FTF Dynamics

The soil profile in CLM4.5 is discretized vertically into 15 layers, and the depth z of a soil layer i is written as follows:

$$z_i = f_s \{ \exp[0.5(i - 0.5)] - 1 \}, \quad (8)$$

where $f_s = 0.025$ is a scaling factor. Then, based on the second law of heat conduction in one-dimensional form, the model calculates the soil temperature for each layer of the 15-layer soil profile, as well as snow temperature for up to five overlying layers of snow. However, the model cannot provide an exact soil depth at which the temperature is 0 °C, which is quite important for diagnosing the evolution of frozen soil as well as the soil carbon-nitrogen processes.

The Stefan equation provides a basis to compute one-directional freeze and thaw in a soil column (Jumikis, 1978). This equation is based on heat conduction and assumes that all heat that reaches the

freezing or thawing front is used for the water freezing or melting. This method has been applied previously to obtain one-directional FTFs in a soil profile (Gao et al., 2016; Xie & Gough, 2013). The FTFs calculation can be described as

$$z_l = \sqrt{\frac{2\lambda(T - T_f)t}{L\theta}}, \quad (9)$$

where z_l is the FTFs depth, l is the frozen interface or thawing front, λ is thermal conductivity, t is the freezing or thawing duration, T is the average temperature at the soil surface, T_f is the freezing/thawing point temperature, L is the volumetric latent heat of fusion, and θ is the volumetric fraction of the soil moisture content. In this study, FTF depths are calculated at a daily time scale.

Assuming that the thickness, depth, and soil thermal conductivity of soil layer i are Δz_i , z_i , and λ_i , respectively, the freeze/thaw index requirement for the FTFs to pass from z_{i-1} to z_i is N_i , the volumetric fraction of the soil moisture in i th soil layer is θ_i , and the thermal resistance of i th soil layer is $R_i = \Delta z_i/\lambda_i$. Then we have

$$\begin{cases} N_1 = (L \cdot \theta_1 \cdot z_1) \left(\frac{R_1}{2} \right), \\ N_2 = (L \cdot \theta_2 \cdot z_2) \left(R_1 + \frac{R_2}{2} \right), \\ \dots \\ N_i = (L \cdot \theta_i \cdot z_i) \left(\sum_{n=1}^{i-1} R_n + \frac{R_i}{2} \right). \end{cases} \quad (10)$$

If the freeze/thaw index $D = (T - T_f) t$ satisfies $D \geq \sum_{n=1}^{i-1} N_n$ and $D < \sum_{n=1}^i N_n$, then

$$D - \sum_{n=1}^{i-1} N_n = (L \cdot \theta_i \cdot z_{f0}) \left(\sum_{n=1}^{i-1} R_n + \frac{z_{f0}}{2\lambda_i} \right). \quad (11)$$

where z_{f0} is the FTF depth in i th soil layer.

By solving equation (11), we can obtain z_{f0} as follows:

$$z_{f0} = -\lambda_i \sum_{n=1}^{i-1} R_n + \left\{ \lambda_i^2 \left[\sum_{n=1}^{i-1} R_n \right]^2 + \left[2\lambda_i \left(D - \sum_{n=1}^{i-1} N_n \right) / (L \cdot \theta_i) \right]^2 \right\}^{1/2}, \quad (12)$$

and hence the FTF depth

$$z_l = z_{i-1} + z_{f0}. \quad (13)$$

The above equations were developed to describe downward freezing/melting, but the same approach was taken to calculate upward freezing/melting. In addition, because this method relies on the soil moisture content and ground temperature (GT), any changes in these variables would give different FTFs. Consequently, any changes induced by HWR or GLF can influence the changes in FTFs.

2.4. A High-Resolution Land Model With GLF, HWR, and FTFs

As noted previously, we incorporated the three schemes of GLF, HWR, and FTFs into CLM4.5 to develop a high-resolution model with GLF, water use, and soil freeze-thaw front dynamics, which is called Land Surface Model for Chinese Academy of Sciences (CAS-LSM). The schematic diagram describing CAS-LSM is shown in Figure 1. CAS-LSM utilized high-resolution basic data sets for vegetation, geographic features, soil texture, and water use, as well as the high-performance computing clusters. The scheme of GLF is based on a quasi-3D GLF model. The HWR processes consist of GW pumping, surface water intake, and water use for livelihood, industry, and irrigation. The scheme of FTF dynamics was incorporated into the soil moisture module in CAS-LSM.

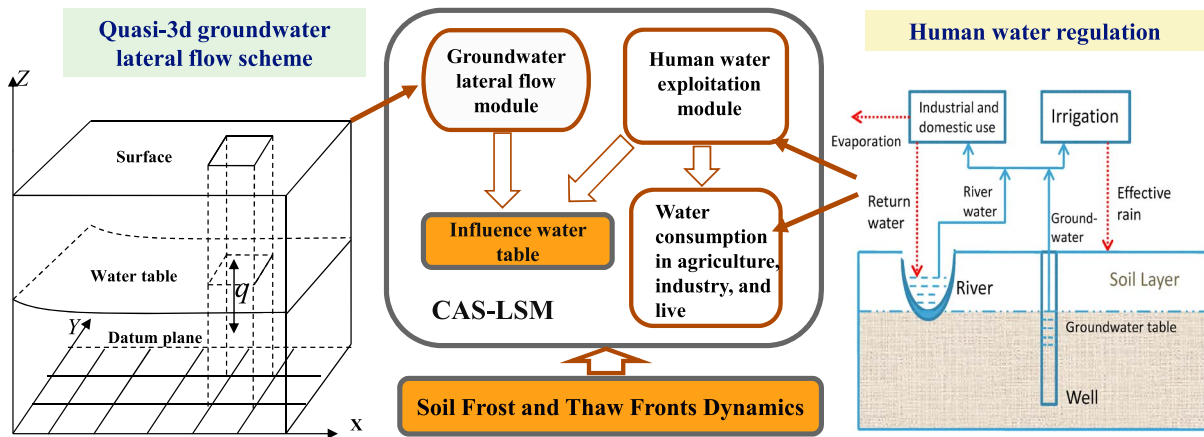


Figure 1. Schematic diagram of the land model CAS-LSM with groundwater lateral flow, human water use and soil freeze-thaw fronts. On the left is the illustration of the quasi-3D groundwater lateral flow; the illustration on the right shows the human water use including groundwater pumping, surface water intake, and water use for livelihood, industry, and irrigation; the middle illustration shows a land surface model coupled with a scheme of soil frost and thaw fronts dynamics.

Figure 2 shows the general calculation process in CAS-LSM and its coupling with GLF, HWR, and FTFs in details. The primarily modified modules are the soil temperature module and the soil hydrology module, which includes the processes of surface runoff, soil water, GW, and river routing. The calculation process can be described as follows:

1. As shown in the blue dashed box in Figure 2, the scheme of FTFs is coupled with the soil temperature module. First, based on the model soil layers and the calculated soil water and ice at the last time-step, we find the 0° location in each soil layer using equation (12). Then the FTF depths in the whole soil column are obtained using equation (13). Meanwhile, the possible redundant energy can be finally put back into the soil to update the soil temperature. The updated soil temperature is used subsequently in the soil hydrology module.

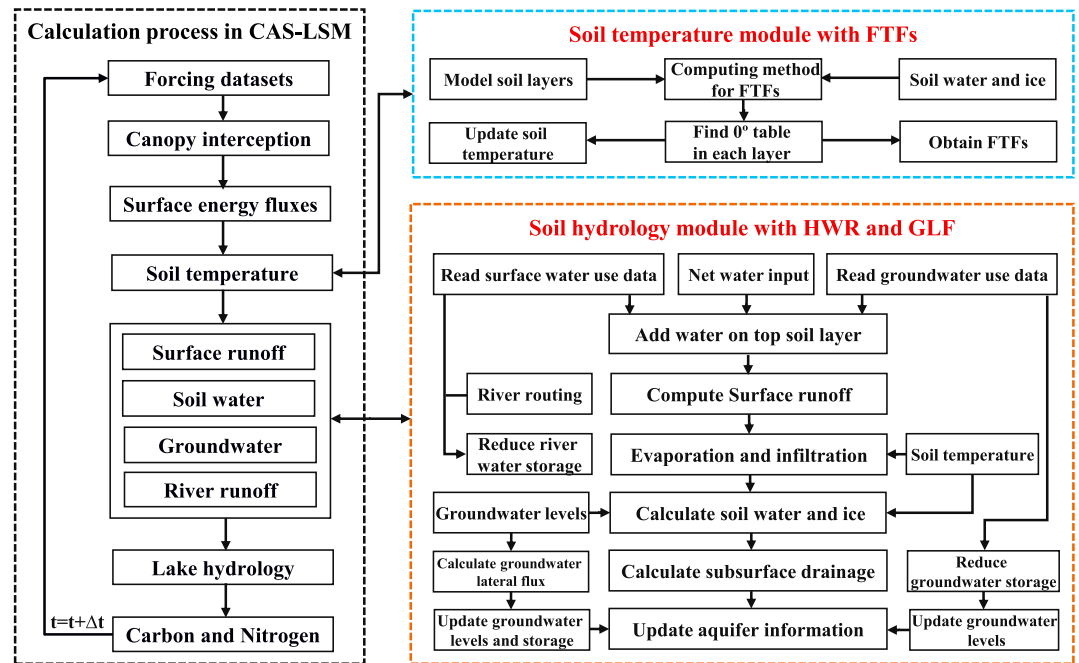


Figure 2. The main calculation process in CAS-LSM and its coupling with GLF, HWR, and FTFs: The content in the black dashed box displays the main calculation process in CAS-LSM; the details in the blue dashed box show how the scheme of FTFs is coupled with the soil temperature module; the details in the orange dashed box show how the schemes of GLF and HWR are coupled with the soil hydrology module.

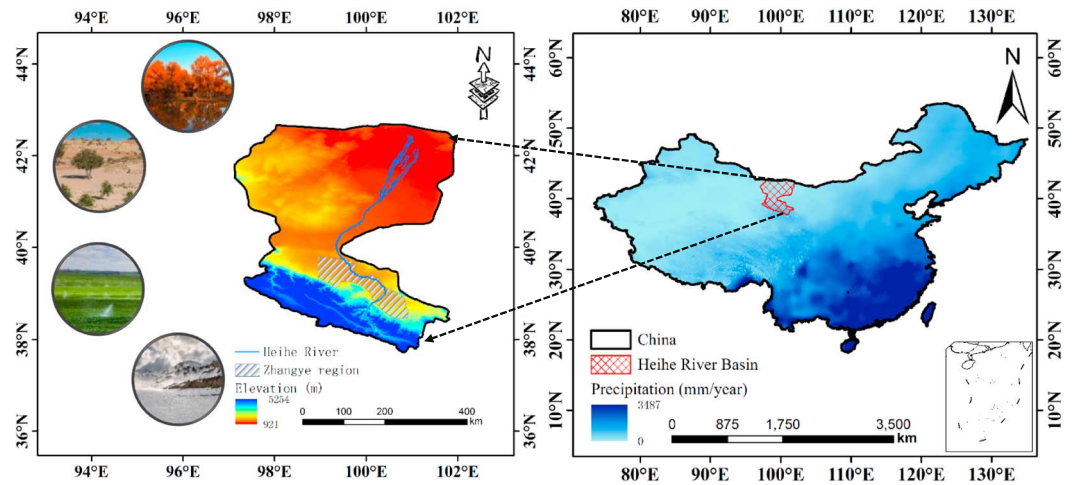


Figure 3. Heihe River Basin: the Heihe River, landscapes, and its location in China. The illustration on the right shows the climatological mean annual precipitation over China, and the region with red grids is the Heihe River Basin, which is located in the arid and semiarid region of northern China. The illustration on the left shows the elevations, Zhangye region (human-dominated zone), and Heihe River in the Heihe River Basin. The encircled pictures show the glacier, oasis, desert, and *Populus euphratica* in sequence from high land (blue color) to low land (red color).

2. As shown in the orange dashed box in Figure 2, the schemes of GLF and HWR are coupled with the soil hydrology module. As input, this module uses not only the calculated variables in other processes, such as the soil temperature and net water input, but also the external data on surface water and GW use. All the irrigation water from both river water and GW is regarded as the net water input on the topsoil layer. These water inputs would participate in the next hydrological computing from surface runoff to subsurface drainage and could have impacts on related land surface factors, such as GT, soil moisture, latent heat flux (LH), and sensible heat flux (SH). Due to the differences in the sources of surface water and GW, different processes of extracting water are included. The amount of surface water use is extracted from river storage using equation (1) and the amount of GW use is extracted from aquifer withdrawal using equation (2). The latter would deepen the depth to the GWT calculated using equation (3). The GLF depends on the current GW levels, which are affected by the water recharge from soil in the vertical hydrological process. Then according to equation (5), the lateral GW flux is calculated. Last, the water levels and GW storage are changed using equations (6) and (7).
3. After returning the prognostic variables to the main process of CAS-LSM, the GLF, HWR, and FTFs change not only the water and energy in the soil process but also the whole land surface processes, which could further affect the climate.
4. Incorporating the GLF, HWR, and FTFs into a land surface model, and the total water balance of the hydrological system can be written as follows:

$$\Delta W_{\text{can}} + \Delta W_{\text{sfc}} + \Delta W_{\text{sno}} + \Delta W_{\text{soil}} + \Delta W_a = (q_{\text{rain}} + q_{\text{sno}} + q_s + q_g + q_{\text{gwlf in}} - ET_{\text{veg,ground,human}} - q_{\text{over}} - q_{\text{h2osfc}} - q_{\text{gwlf out}} - q_{\text{rgwl}} - q_{\text{ice}}) \Delta t, \quad (14)$$

where the left side of equation (14) denotes the changes in canopy water, surface water, snow water, soil water and ice, and water in the unconfined aquifer in turn. The variables in the parentheses on the right side denote, in turn, the water fluxes for the liquid part of precipitation, the solid part of precipitation, the surface water, GW evapotranspiration (ET) from both vegetation and soil, surface runoff, runoff from surface water storage, subsurface drainage, and other runoff from glaciers, lakes, and wetlands. The q_s and q_g used for irrigation, domestic purposes, and industry, most of which would return to soil. ET also were modified because some water used for domestic purposes would directly return to the atmosphere by dissipation.

Table 1
Basic Forcings for Model Runs

Basic data	Resolution	Time	Source
ITPCAS forcing	0.1°/3 hr	1981–2012	(Yang et al., 2010)
CLDAS forcing	0.0625°/3 hr	2013	(Jia et al., 2013; Shi et al., 2011)
Land cover	1 km	2000	(Ran et al., 2012)
Soil data set	1 km	2012	(Dai et al., 2013)
Irrigation data set	1 km	1981–2013	(Zeng et al., 2017)

3. Simulations

3.1. Study Area

The endorheic HRB in China was used as the study area, and simulations using the CAS-LSM model were conducted. As shown in Figure 3, the HRB, located at 98°E–102°E and 37°N–42°N, covers a total area of 143,000 km² and is the second largest inland river basin in northwestern China. Water that flows from the headwater to the downstream controls the landscape. Glaciers and permafrost are present in the high-mountain areas, while forests and alpine meadows cover the middle-mountain regions. A desert-oasis-river landscape occurs in the middle and lower basin reaches, with well-developed agriculture in the midstream and a riparian ecosystem distributed downstream along the river. In the upstream basin, the mean annual precipitation is approximately 300–700 mm with distinct vertical zonal divisions. The upper reaches of the HRB contain nearly the entire water resource of the whole basin (Wu et al., 2010). In the middle reaches, the elevation decreases from 2,000 to 1,000 m and the annual precipitation correspondingly decreases from south to north from 200 to <100 mm (Li et al., 2001). The lower reaches have an average elevation of 1,000 m and constitute an arid region with a mean annual precipitation of 42 mm, according to statistical data gathered from meteorological stations and simulations from regional climate models (Xiong & Yan, 2013). This basin has experienced severe water shortages and environmental deterioration (Cheng et al., 2014). Recently, the Heihe Watershed Allied Telemetry Experimental Research (HiWATER) program (Li et al., 2013) was launched to find a scientific way of supporting sustainable environmental management.

3.2. Data and Experimental Setup

Some basic data sets used for land model simulations are listed in Table 1. The atmospheric forcing data set (Institute of Tibetan Plateau Research, Chinese Academy of Sciences [ITPCAS], forcing) from 1981 to 2012 was acquired as described in Yang et al. (2010), with a spatial resolution of 0.1° and a temporal resolution of 3 hr. We extended the coverage of this data set to 2013 using China Meteorological Administration Land Data Assimilation System (CLDAS) forcing (Jia et al., 2013; Shi et al., 2011). To satisfy the high-resolution process, we replaced the CLM4.5 land cover data with the Multi-source Integrated Chinese Land Cover map available at a 1-km resolution (Ran et al., 2012). We used the land cover map with 30-m resolution (Li et al., 2013; Zhong et al., 2015) to identify the specific crop types for each crop grid cell. The soil data set included in the CLM4.5 model was replaced with the China Soil Characteristics Dataset with a 1-km resolution (Dai et al., 2013). We used the 1-km monthly irrigation data sets (from both GW and river water) as the model input, provided

Table 2
Data for Model Validation

Data	Resolution	Time	Source
GWT depth	site	Climatological mean	(Zhou et al., 2011)
Evapotranspiration	1 km	2001–2011	(Wu et al., 2010)
Latent heat flux	site	2013	(Li et al., 2013; Liu et al., 2011)
Sensible heat flux	site	2013	
Ground temperature	site	2013	
FTFs depth	site	2011–2012	(Chen et al., 2014)
Permafrost distribution I	1:10,000,000	2000	(Brown et al., 2002)
Permafrost distribution II	1:4,000,000	2000	(Wang, 2006)

Table 3
Experimental Setup

Group name	Resolution	Simulation period	Activated modules
EXP1	0.0083°	1981–2013	GLF
EXP2	0.0083°	1981–2013	GLF + HWR
EXP3	0.0083°	1981–2013	GLF + HWR + FTFs

by the Cold and Arid Regions Science Data Center at Lanzhou (Zeng, Xie, & Liu, 2017). These data were developed based on the local statistical data from a water resources bulletin, which reflects the actual water consumption in the study area.

As shown in Table 2, we collected the measured GWT depths from 81 observation wells (Zhou et al., 2011). The remote sensing ET data from 2001 to 2011 were extracted from the ETWatch model, which is a system for monitoring regional ET (Wu et al., 2010). The collected LH, SH, and GT in 2013 from eddy covariance and automatic weather monitoring systems were obtained from the hydrometeorological observation network conducted by the HiWATER program (Li et al., 2013; Liu et al., 2011). Daily FTF data from 2011 to 2012 for the Hulugou station in the HRB were obtained from the Cold and Arid Regions Science Data Center at Lanzhou (Chen et al., 2014), as were two data describing the spatial pattern of permafrost. The data on the spatial distribution of permafrost were extracted based on the works of Brown et al. (2002) and Wang (2006).

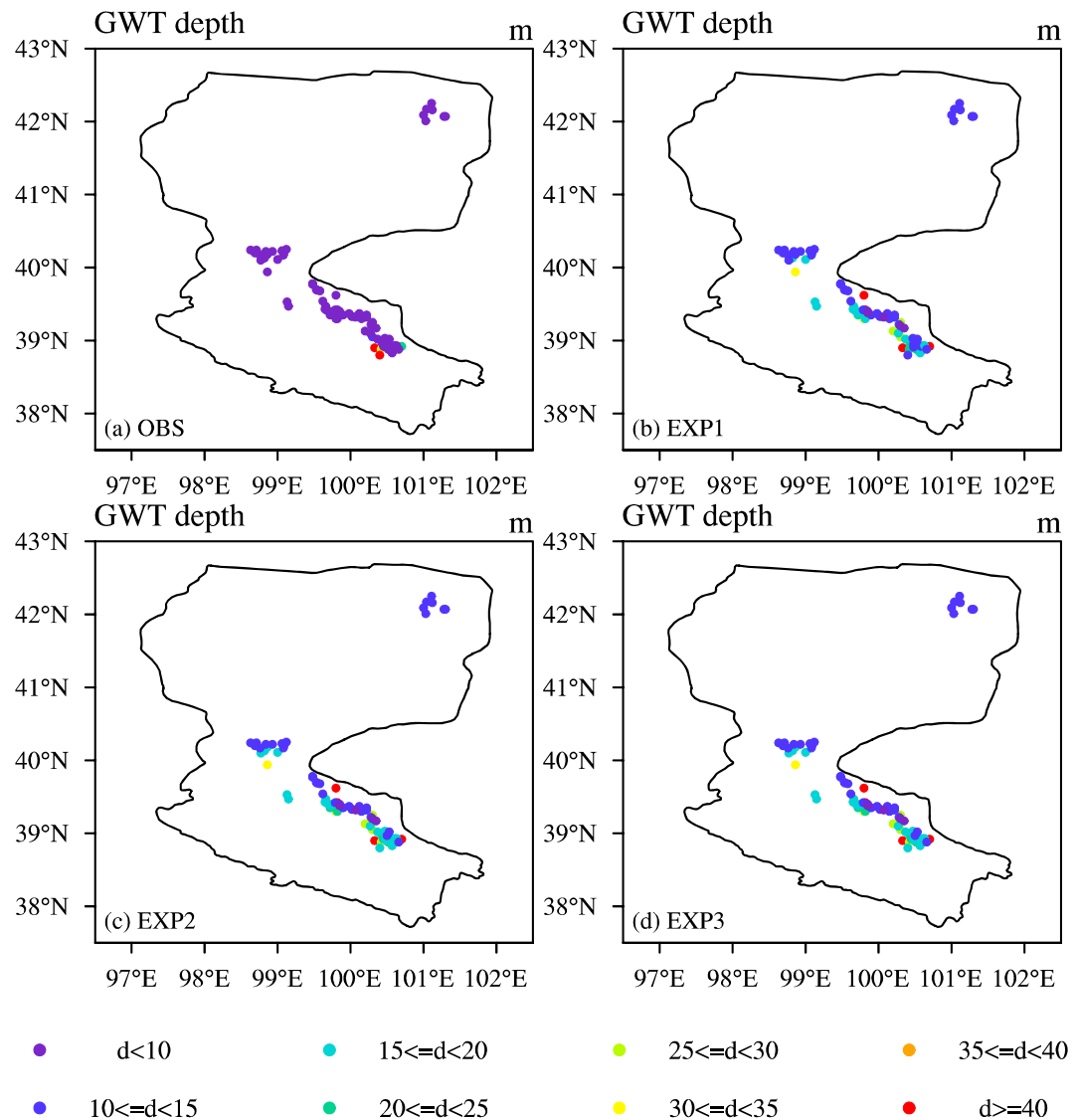


Figure 4. Spatial distributions of the multiyear averaged GWT depths by observation at (a) 81 sites, and modeling results from (b) EXP1, (c) EXP2, and (d) EXP3.

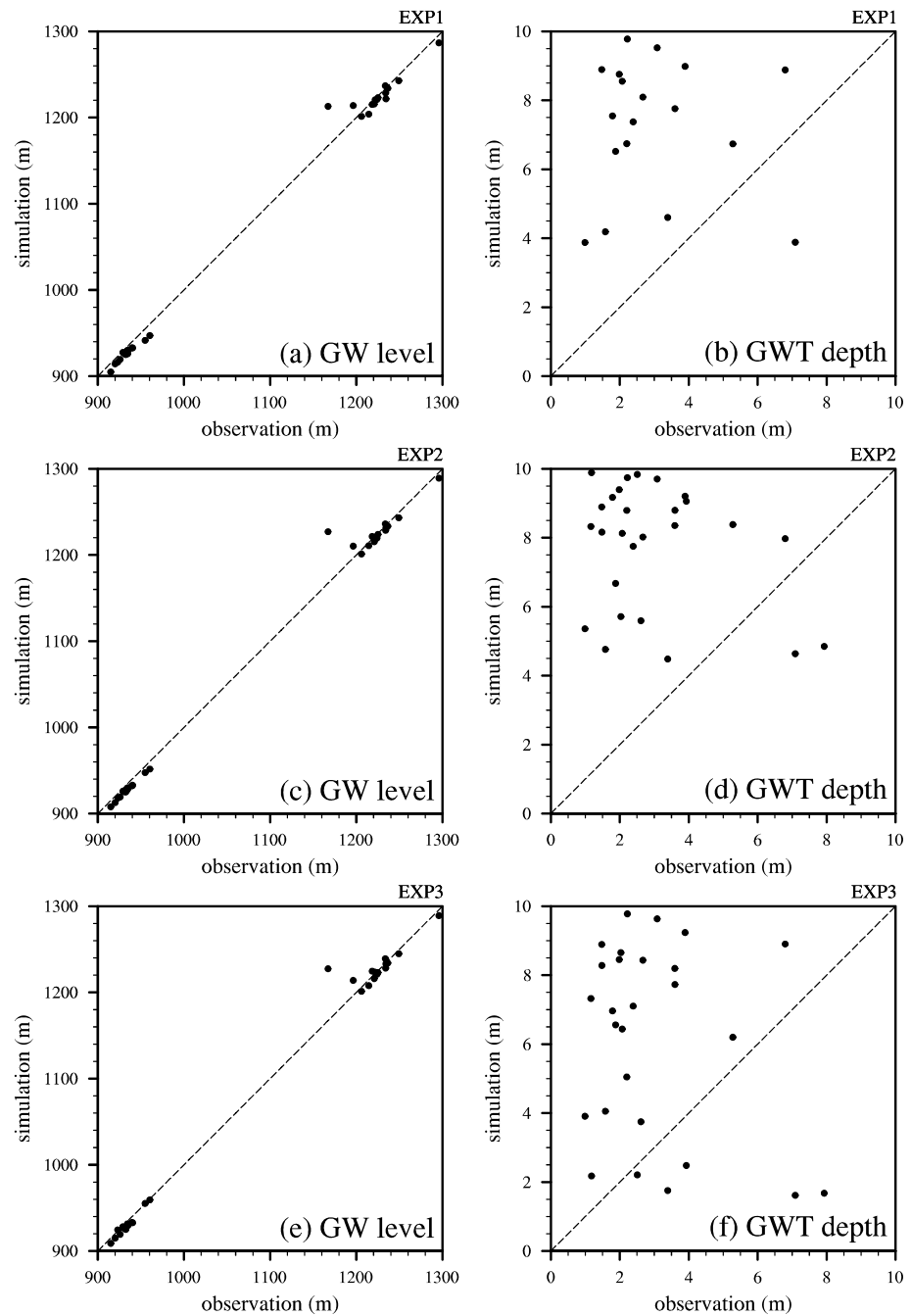


Figure 5. Scatter plots for comparing simulated shallow groundwater level and depth from (a and b) EXP1, (c and d) EXP2, and (e and f) EXP3 with the observed data.

Three simulations were conducted using CAS-LSM, as shown in Table 3. All simulations were conducted with the fully prognostic carbon and nitrogen cycle modules accompanied by the crop module. The first simulation (EXP1) activated the GLF module only. The second simulation (EXP2) used only the GLF and HWR modules and was conducted to account for responses of GW resources to human activity. The last simulation (EXP3) activated the GLF, HWR, and FTFs. In this paper, EXP1 including GLF only was considered as the baseline. The model spatial resolution was fixed at 30 arcsec (~1 km). The simulation period (at a time step of 1,800 s) covers from 1981 to 2013, corresponding to a period during which the input data on irrigation were available.

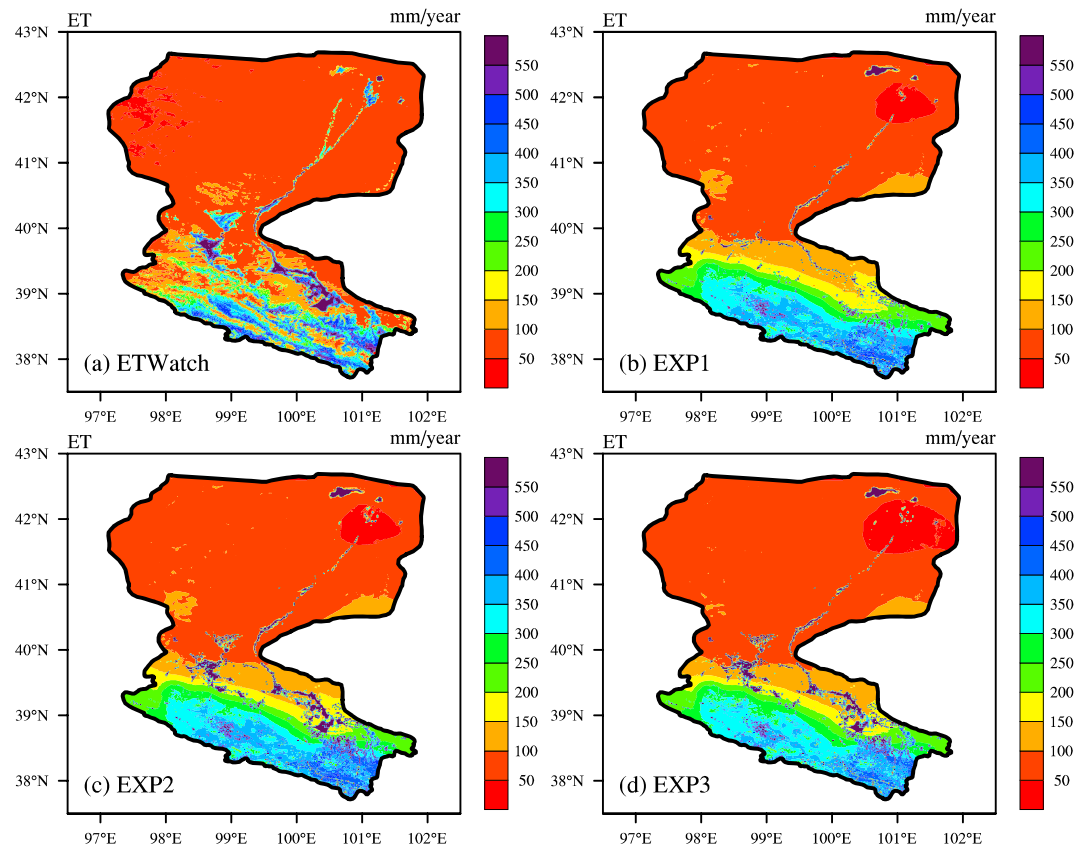


Figure 6. Spatial distribution of climatologic states for evapotranspiration from (a) remote sensing, and simulations from (b) EXP1, (c) EXP2, and (d) EXP3.

3.3. Validation

Figure 4 shows that from the perspective of simulating the spatial distribution of GWT depths. Compared with observations at well sites, all the integrated model simulations (EXP1, EXP2, and EXP3) could well fall into the range of the measured GWT depths. Some observations were overestimated in the human-dominated zone of the middle reaches where the disturbance induced by irrigation was much more intensive than in other places. Figure 5 displays the comparisons between simulated shallow GW level and GWT depth from EXP1, EXP2, and EXP3 and the observed data. We found that the simulated water levels look satisfactory, and more results from EXP3 than the other simulations are close to the 1:1 diagonal line, which may indicate that the model in EXP3 is a little better than the models in EXP1 and EXP2 for GWT depth modeling.

Remote sensing data can describe the spatial variation of some hydrological processes over a large area better than ground observations. Figure 6 shows that compared to the model without HWR, the two models with HWR better simulated the spatial pattern of multiyear mean annual ET, especially for the regions with intensive human activities. In the middle reaches of HRB, intensive irrigation resulted in $ET > 500$ mm/year, much higher than that in other places. However, for ET modeling, the EXP3 simulation did not improve the estimates significantly compared to those in the previous simulations. Nevertheless, EXP3 simulation was made using the revised model that was newly coupled with the scheme describing the change in FTFs, which could boost the accuracy of the soil temperature simulation (Gao et al., 2016).

Then we validated the new model by the eddy covariance method and using automatic weather station data from three observation stations located in the upper, middle, and lower reaches of HRB. LH from the three simulations were compared with field measurements in Figures 7a–7c. The simulated results accorded well with observations at the Gobi and Luodi stations, while there were considerable errors at the Arou station during the latter half of the year. Figures 7d–7f show that the model could simulate the observed seasonal

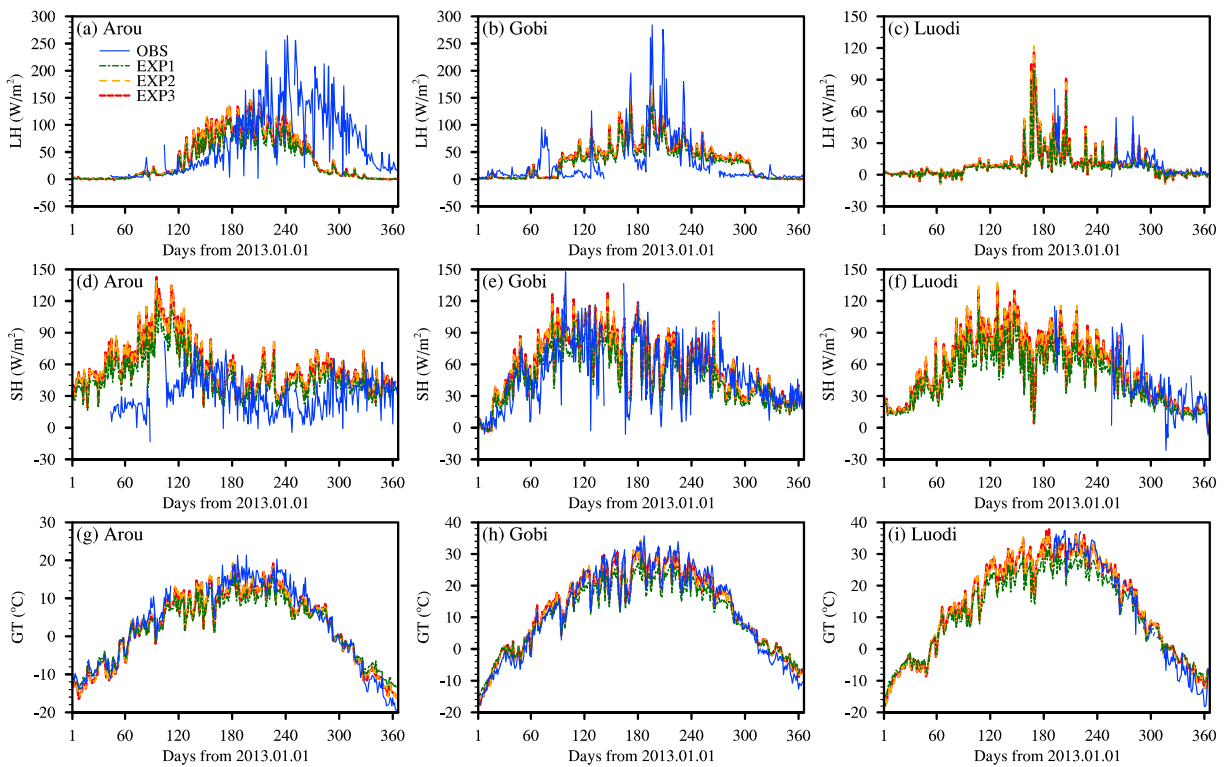


Figure 7. Time series of daily (a–c) sensible heat flux, (d–f) latent heat flux, and (g–h) ground temperature from observations at Arou, Gobi, and Luodi and simulations from EXP1, EXP2, and EXP3 during 2013.

change of SH at all three sites, with slight overestimation in spring at the Arou station. The GT was precisely simulated during the whole year in Figures 7g–7i. In general, while all the experiments could reflect the seasonal change in LH, SH, and GT, the simulations with HWR (EXP3 and EXP2) were closer to the limited observations (black line).

In addition, one of the highlights in the CAS-LSM model is the detection of the depths of soil freezing and thawing in the frozen soil regions. To test the model performance in simulating these features, we conducted a validation at the Hulugou site, which is located in an area in the HRB having seasonally frozen soil. Figure 8 shows that the simulated FTF depths agree well with the observed data. The correlation coefficients of the simulations for the frost front and thaw front are 0.82 and 0.77, respectively, and the root-mean-square errors are 0.68 and 0.77 m, respectively. Figure 8 also illustrates the seasonal cycle of freeze and thaw fronts. As the colder season begins, the frost front moves from the soil surface to deep into the soil profile before thawing begins. In the thawing period, the depth of the thaw front increases and reaches the location of the frost, and finally, the soil thaws completely.

In this paper, the distribution of permafrost could be calculated based on simulated FTF depths. If the maximum soil thaw depth in summer was less than the maximum frost depth in winter, the soil was defined as permafrost and the maximum soil thaw depth was called the active layer thickness (ALT). To evaluate the performance of simulating the distribution of permafrost, we also compared the simulated climatological distribution of permafrost with the surveyed maps. Figure 9 shows that the simulated pattern (with a total permafrost area of 24,534 km²) in Figure 9a is most similar to the observed pattern (having an area of 18,957 km²) provided by Wang (2006) in Figure 9c. However, both of these permafrost areas are less than that (32,603 km²) given by Brown et al. (2002) that is shown in Figure 9b. This difference may have been due to different research scales in the investigations. The data from Brown et al. (2002) were extracted from the circum-Arctic map of permafrost and ground-ice conditions and are probably appropriate for studying global changes in permafrost. On the contrary, the data from Wang (2006) were based on high-resolution observations and field surveys in China and are more appropriate for the permafrost research in some regions of

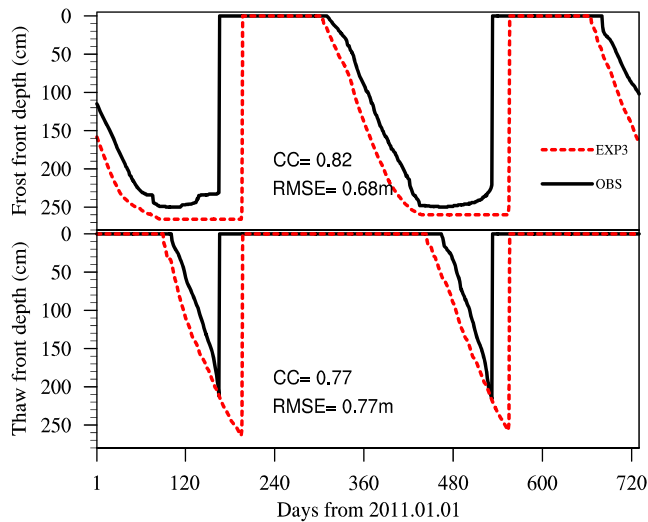


Figure 8. Time series of observed and simulated daily soil frost and thaw front depths at Hulugou site in the Heihe River Basin from 2011 to 2012.

China, such as HRB. In general, based on the validations in this study that supplemented previous tests (Zeng, Xie, Yu, Liu, Wang, Jia, et al., 2016; Zeng, Xie, Yu, Liu, Wang, Zou, et al., 2016; Zeng, Xie, & Liu, 2017), CAS-LSM can be considered as a satisfactory tool for studying land processes, especially in cold and arid regions experiencing intensive human activity.

3.4. Temporal and Spatial Pattern of FTFs

Having distinguished the areas of permafrost and seasonally frozen soil, we found permafrost to be located in the upstream region of HRB, and the seasonally frozen soil mainly in the middle and lower reaches of HRB. We checked the maximum frost depths distributed across the seasonally frozen areas and the ALTs across the permafrost area. Figure 10a shows that the deepest frost front ranged from 1 to 3 m below the soil surface. The deepest monthly mean frost front often occurred in April. The averaged frozen depth of approximately 1.8 m in the human-dominated region in the middle reaches of HRB was obviously shallower than that in other places (mean depth 2.6 m). This difference may be attributed to the complex human activities, such as land cover change and crop planting, which may change the thermal conductivity of soil.

Figure 10b illustrates that most of the ALTs were approximately 2.1 m, but could reach more than 2.7 m in some places. During the 30-year study period, as shown in Figures 10c and 10d, the maximum frost front depths decreased in the east at an average rate of

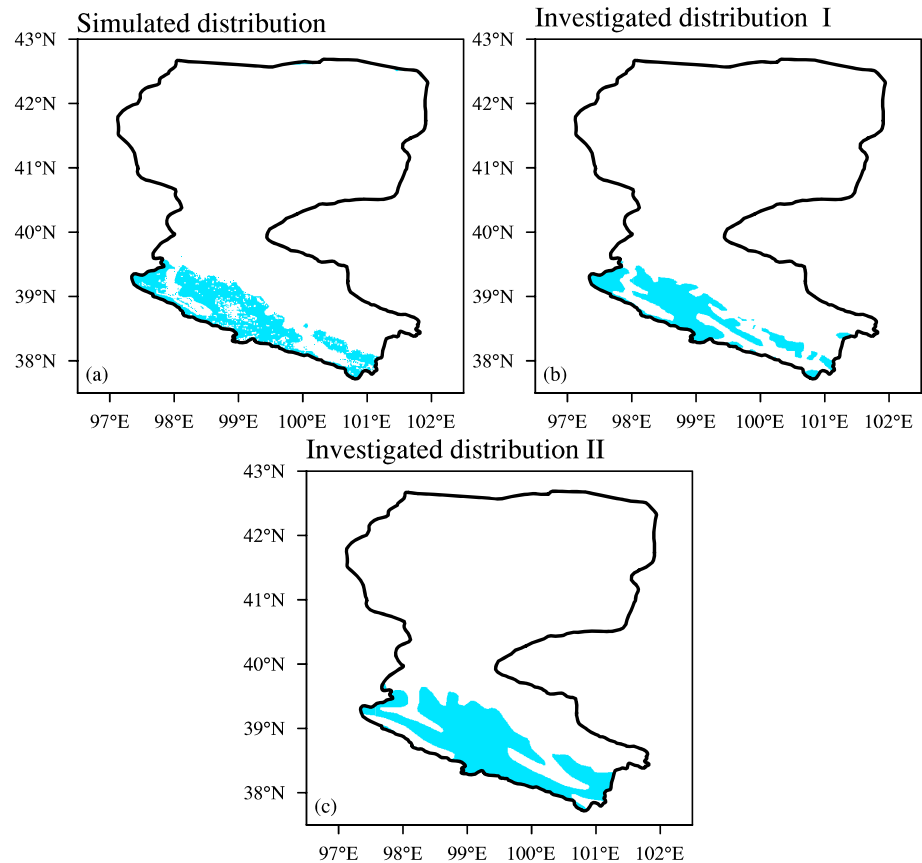


Figure 9. Spatial distribution of the permafrost in the Heihe River Basin: (a) the nearly 30-year averaged result from EXP3, (b) the data extracted from the circum-arctic map of permafrost and ground-ice conditions by Brown et al. (2002), and (c) the data investigated based on field survey and remote sensing by Wang (2006).

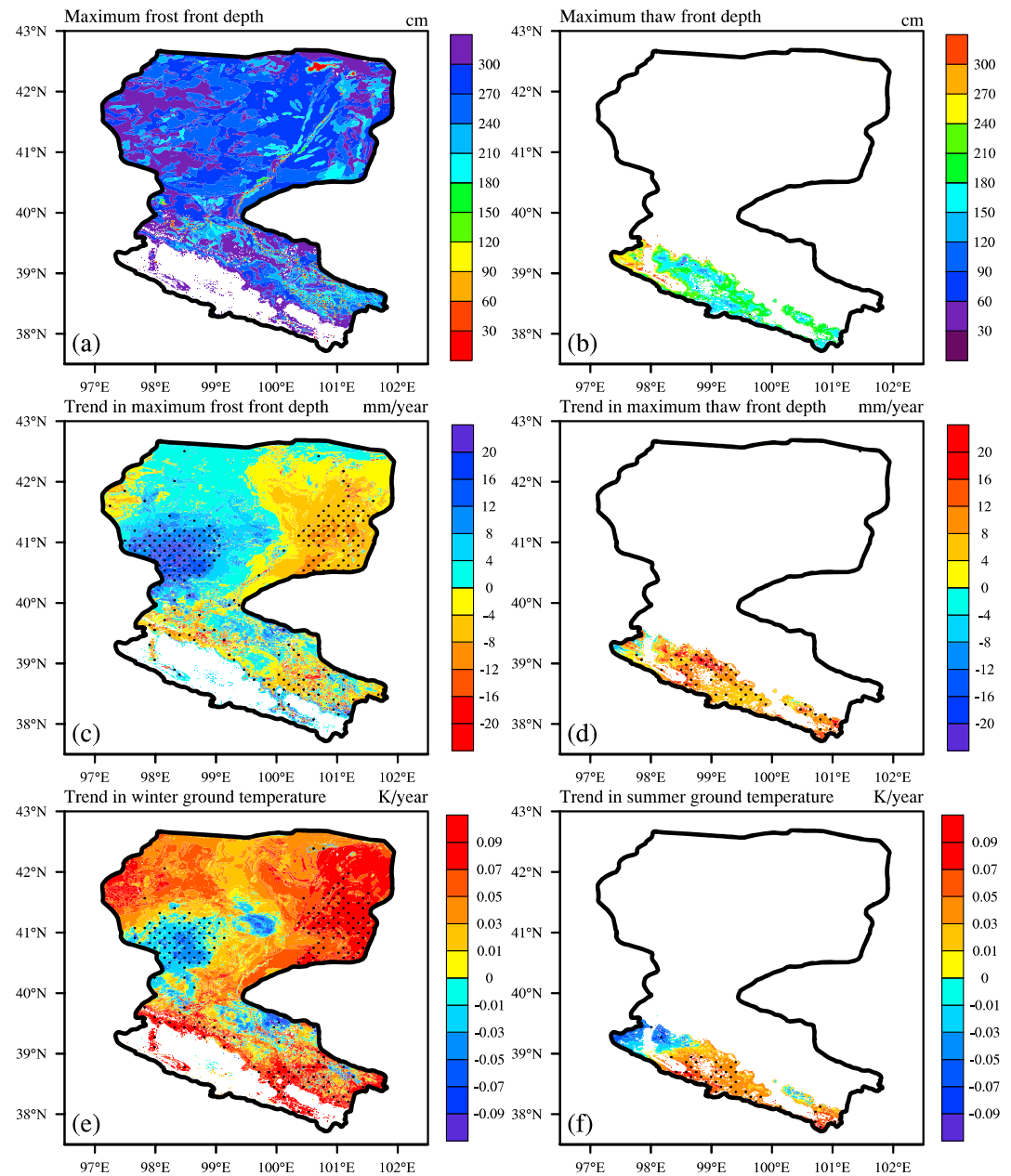


Figure 10. Spatial distribution of the climatologic states for (a) maximum frost front depths and (b) maximum thaw front depths and the near 30-year trends in (c) maximum frost front depths, (d) maximum thaw front depths, (e) ground temperature in winter, and (e) ground temperature in summer.

approximately 5 mm/year and increased in the west at the rate of 10 mm/year. Furthermore, the ALT increased over most of the permafrost region at a mean rate of 6 mm/year.

GT plays a critical role in the modeling of FTFs. To understand the change in FTFs, we also examined the change in GTs. Figure 10e shows that the GT in winter increased over most part of the seasonally frozen soil region. However, GT decreased in the west, which was in accord with the deeper soil frost front, although the trend in GT did not pass significance testing. Figure 10f shows that the GT in summer increased in permafrost areas, where the ALT increased as well.

We also inspected the trends in spatially averaged annual FTFs in permafrost areas, seasonally frozen soil areas, and areas dominated by human activities. Figure 11a shows that the air temperature in each area

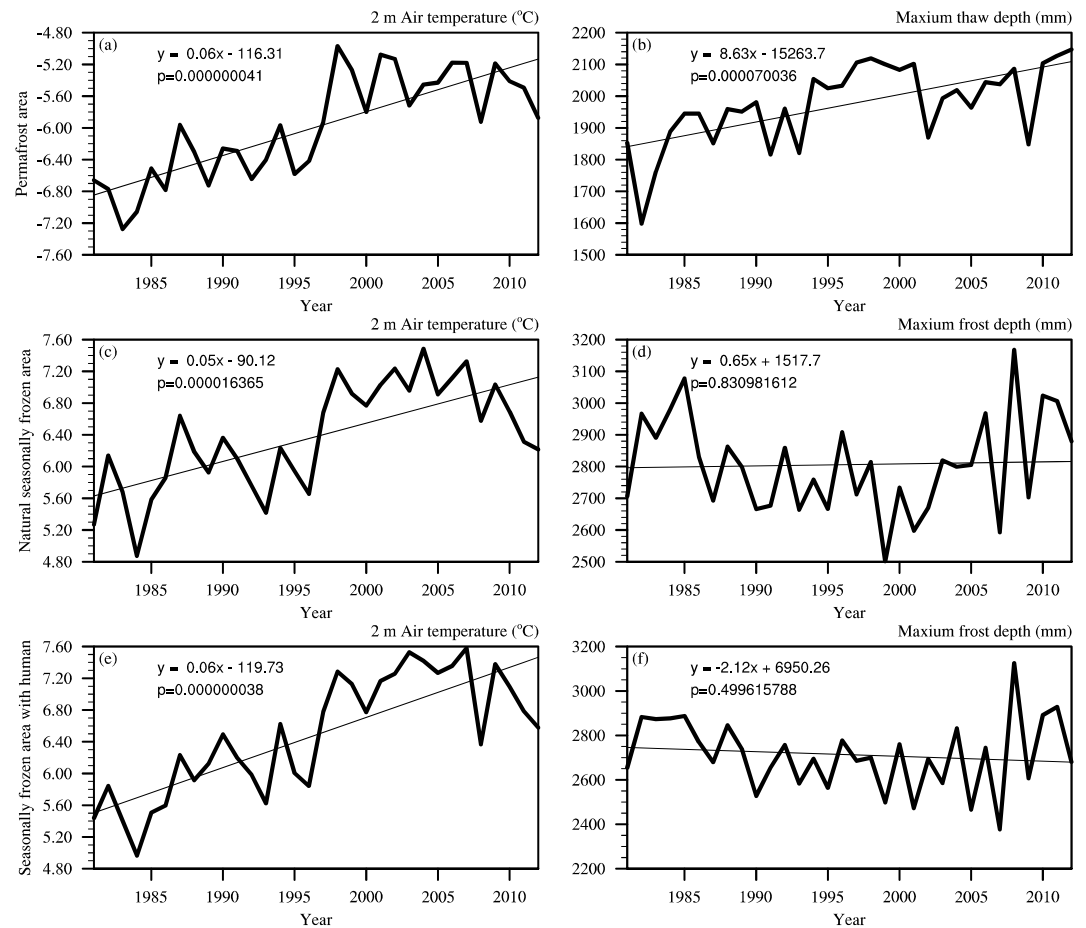


Figure 11. Interannual variations in frozen soil in permafrost areas, natural areas of seasonally frozen soil, and the human-dominated areas from 1981 to 2012 (results from EXP3).

rose from 1981 to 2012 at an almost identical rate of 0.06 mm/year. Figure 11b shows the maximum thaw depth increased at the rate of 8.63 mm/year in permafrost areas. The shallowest thaw front occurred in 1982 and the deepest occurred in 2012. Figure 11d indicates that the maximum frost depth changed only slightly in areas of seasonally frozen soil without human activity. Figure 11c shows that the maximum frost depth increased in nearly half of the areas of seasonally frozen soil that were not dominated by human activity and decreased in the other half, so that the spatially averaged frost depth appeared to be stable.

Figure 11f shows that the maximum frost depths decreased at a rate of 2.12 mm/year in the human-dominated areas, where the shallowest frost front occurred in 2007 and the deepest occurred in 2008. These changes may support the belief that human water use can hamper the soil freezing process. It is also distinct that the changes in the soil thaw front in permafrost areas were larger than the frost front in areas of seasonally frozen soil. In general, in the context of global warming, the permafrost is being degraded and the change in seasonally frozen soil shows an evident spatial variability in HRB.

3.5. Temporal Trend in Land-Atmosphere Exchange of Carbon, Water, and Energy

Quantifying the hydrological and ecological evolutions in the permafrost region is important for regional environmental management and social development. We checked the annual changes in land-atmosphere exchange of carbon, water, and energy in the permafrost areas in HRB from 1981 to 2012 (Figure 12). The forcing data show that precipitation, including rainfall and snow, increased 3.4 mm/year. With the increasing precipitation and air temperature, ET changed with a similar trend. Accordingly, LH increased and SH decreased. Furthermore, the carbon use efficiency decreased slightly. The change in net ecosystem exchange (NEE) showed that in most years the permafrost region of HRB acted as a carbon sink, and that increasing

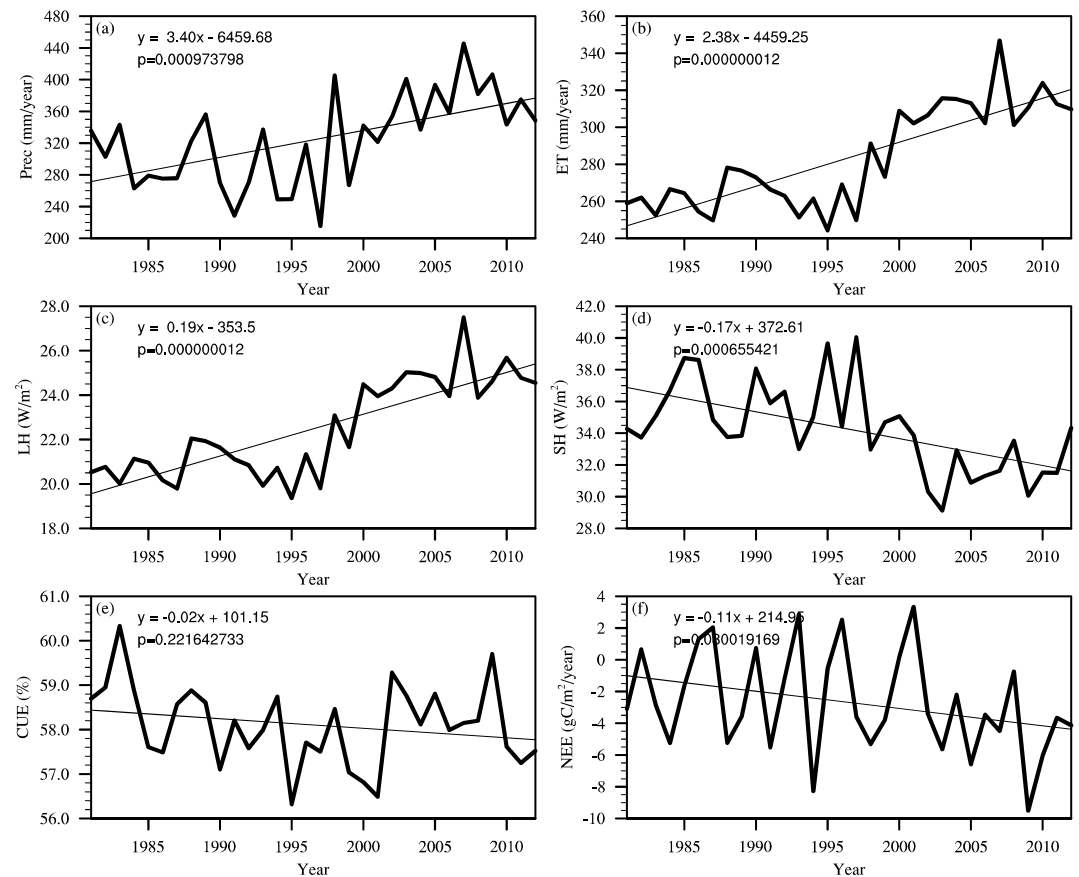


Figure 12. Interannual variations in land-atmosphere exchange of (a) precipitation, (b) evapotranspiration, (c) latent heat flux, (d) sensible heat flux, (e) carbon use efficiency, and (f) net ecosystem exchange over the permafrost zone from 1981 to 2012 (results from EXP3).

amounts of carbon were fixed into the terrestrial ecosystem. That may have been due to the enhanced photosynthesis against the background of warming and wetting (Xie et al., 2016).

Human activities have largely influenced both hydrological and ecological evolution, as well as regional and global climate (Zeng, Xie, & Zou, 2017; Zou et al., 2014). The Zhangye region shown in Figure 3 is a human-dominated region in the HRB. Figure 13 shows the annual changes in the land-atmosphere exchange of carbon, water, and energy over the human-dominated areas, which are located in areas of seasonally frozen soil within the HRB. The precipitation increased by 1.11 mm/year, which was a smaller increase than that in the permafrost zone, which belongs to upstream region with more precipitation than other areas of the basin (Xiong & Yan, 2013). The ET, LH, and SH changed similarly to that in the permafrost zone. However, the carbon use efficiency and NEE changed only slightly over the 30-year study period because of the lasting and stable amount of human water use and crop growth.

In Figures 14a and 14b, with human water use, the multiyear averaged LH has increased by about 60% and the SH has decreased by about 15%. Furthermore, during the nearly 30 years of records, the impacts of water use on LH and SH have increased by 0.02 W/m²/year and decreased by 0.01 W/m²/year, respectively. Figure 14d shows that irrigation may have caused gross primary productivity and net primary productivity to increase, which reduced NEE and meant more carbon was fixed by crop biomass. The impact on NEE became increasingly obvious because this factor increased 0.05 g/m²/s/year.

In addition, the river discharge is an important indicator of the availability of water for the ecosystem in the middle and lower reaches of HRB. Conflicts between agricultural water demand and ecological water requirements have long prevailed in HRB. In Figure 14c, data based on a river segment between the Caotanzhuang

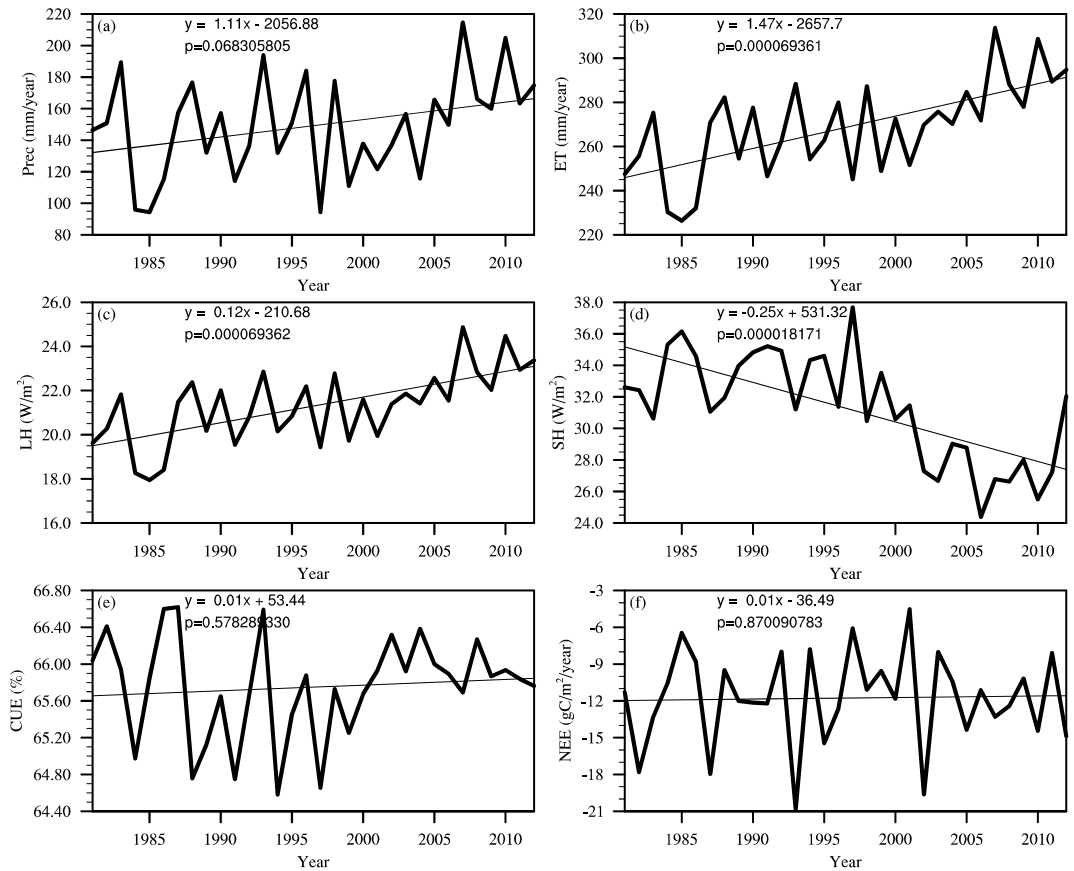


Figure 13. Interannual variations in land-atmosphere exchange of (a) precipitation, (b) evapotranspiration, (c) latent heat flux, (d) sensible heat flux, (e) carbon use efficiency, and (f) net ecosystem exchange over the human-dominated zone from 1981 to 2012 (results from EXP3).

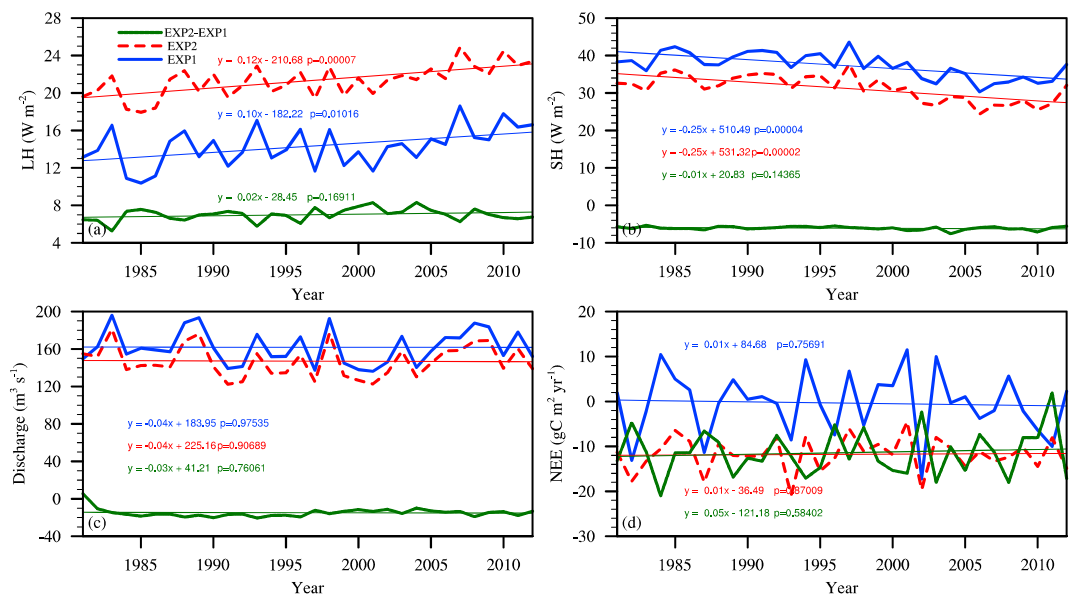


Figure 14. Effects of human water use on (a) latent heat flux, (b) sensible heat flux, (c) river discharge, and (d) net ecosystem exchange in the human-dominated zone from 1981 to 2012 (results from EXP2 and EXP1).

site and Tielu Bridge (which is the lower reach where people extract water) show that human water use reduced the river discharge flowing to the ecological zone in the lower reaches of HRB, though the surface and subsurface runoff can appropriately recharge the river (Zeng, Xie, Yu, Liu, Wang, Jia, et al., 2016). This observation is in accord with previous discharge estimates for channel sections in the middle reach of the Heihe River (Liu et al., 2016).

3.6. Limitations of this Study

The model CAS-LSM should more carefully consider the linkage between the GWT and FTFs. For example, the location of the frozen table would impact the soil moisture by raising and lowering the GWT (Wang et al., 2006). For a regional application, tuning of model parameters is necessary, which is supposed to be implemented based on data from long-term comprehensive observation networks (Li et al., 2013). Due to the limitation of long-term observation and the huge computing cost of CLM with activated C-N and crop modules, an efficient parameter optimization method has not been found; therefore, some simulated results could not be accurately matched with the observations. In addition, HWR is also related to the local economy which would update the water allocation through the policy (Cheng et al., 2014; Zhang et al., 2018). How to introduce the impacts of social economy into the model is a big challenge. The modeling uncertainties can be quantified by ensemble simulations (Ajami et al., 2007; Duan et al., 2007). We also did not analyze the interactions between either two of the new processes at a finer temporal scale in the study area due to limitation of available data.

4. Conclusions

In this work, a land surface model CAS-LSM was developed by incorporating synchronously the mathematical descriptions of GLF, HWR, and FTFs into a CLM to investigate the interactions between GW, soil freezing and thawing process, and human water use. Numerical simulations of the period 1981–2013 using CAS-LSM with 1-km resolution were conducted for the HRB in China.

Compared with observations, CAS-LSM reproduced the distributions of GW, ET, and permafrost reasonably and well matched the temporal changes in GT, heat fluxes, and FTFs. Results illuminate the temporal and spatial characteristics of frozen soil and the changes in the land-atmosphere exchange of carbon, water, and energy. The permafrost and seasonally frozen soil were distinguished. In the seasonally frozen areas, the maximum soil frost depth increased by 0.65 mm/year within natural areas and decreased by 2.12 mm/year in human-dominated areas. The ALT increased 8.63 mm/year for permafrost. In the permafrost zone ET and LH increased, and the SH declined. In the human-dominated areas water use raised the LH and reduced the SH, NEE, and streamflow recharging to the eco-fragile region in the lower reaches.

Results suggested that CAS-LSM is a potential tool for studying land surface processes, especially in cold and arid regions experiencing human interventions. Because CAS-LSM can be directly used as the land model of climate system models, we will present some results in the next work, using a climate system model coupled with the proposed land surface model to investigate the interactions between the land and the atmosphere at large scales.

Acknowledgments

This work was jointly supported by the National Natural Science Foundation of China (NSFC) project “Integrated modeling of the water-ecosystem-economy system in the Heihe River Basin” (grants 91125016 and 41575096) and by the Key Research Program of Frontier Sciences, Chinese Academy of Sciences (CAS), grant QYZDY-SSW-DQC012. Most of the data used in the study were provided by the NSFC data center as part of the major research plan entitled “Integrated research on the eco-hydrological process of the Heihe River Basin” (<http://www.heihedata.org>). We also thank the National Supercomputing Center of Tianjin, China, for use of the supercomputer Tianhe-1.

References

- Ajami, N. K., Duan, Q., & Sorooshian, S. (2007). An integrated hydrologic Bayesian multimodel combination framework: Confronting input, parameter, and model structural uncertainty in hydrologic prediction. *Water Resources Research*, 43, W01403. <https://doi.org/10.1029/2005WR004745>
- Bear, J. (1972). *Dynamics of fluids in porous Media* (pp. 361–373). New York: American Elsevier.
- Brown, J., Ferrians, O. J., Jr., Heginbottom, J. A., & Melnikov, E. S. (2002). Circum-Arctic map of permafrost and ground-ice conditions, edited by C. U. N. S. a. I. D. C. Boulder.
- Chen, R., Song, Y., Kang, E., Han, C., Liu, J., Yang, Y., et al. (2014). A cryosphere-hydrology observation system in a small alpine watershed in the Qilian Mountains of China and its meteorological gradient. *Arctic, Antarctic, and Alpine Research*, 46(2), 505–523. <https://doi.org/10.1657/1938-4246-46.2.505>
- Cheng, G., Li, X., Zhao, W., Xu, Z., Feng, Q., Xiao, S., & Xiao, H. (2014). Integrated study of the water-ecosystem-economy in the Heihe River Basin. *National Science Review*, 1(3), 413–428. <https://doi.org/10.1093/nsr/nwu017>
- Cheng, G., & Wu, T. (2007). Responses of permafrost to climate change and their environmental significance, Qinghai-Tibet Plateau. *Journal of Geophysical Research*, 112, F02S03. <https://doi.org/10.1029/2006JF000631>
- Dai, Y., Shangguan, W., Duan, Q., Liu, B., Fu, S., & Niu, G. (2013). Development of a China dataset of soil hydraulic parameters using pedo-transfer functions for land surface modeling. *Journal of Hydrometeorology*, 14(3), 869–887. <https://doi.org/10.1175/JHM-D-12-0149.1>

- De Graaf, I., Van Beek, L., Wada, Y., & Bierkens, M. (2014). Dynamic attribution of global water demand to surface water and groundwater resources: Effects of abstractions and return flows on river discharges. *Advances in Water Resources*, *64*, 21–33. <https://doi.org/10.1016/j.advwatres.2013.12.002>
- Duan, Q., Ajami, N. K., Gao, X., & Sorooshian, S. (2007). Multi-model ensemble hydrologic prediction using Bayesian model averaging. *Advances in Water Resources*, *30*(5), 1371–1386. <https://doi.org/10.1016/j.advwatres.2006.11.014>
- Fan, Y. (2015). Groundwater in the Earth's critical zone: Relevance to large-scale patterns and processes. *Water Resources Research*, *51*, 3052–3069. <https://doi.org/10.1002/2015WR017037>
- Frauenfeld, O. W., Zhang, T., Barry, R. G., & Gilichinsky, D. (2004). Interdecadal changes in seasonal freeze and thaw depths in Russia. *Journal of Geophysical Research*, *109*, D05101. <https://doi.org/10.1029/2003JD004245>
- Gao, J., Xie, Z., Wang, A., & Luo, Z. (2016). Numerical simulation based on two-directional freeze and thaw algorithm for thermal diffusion model. *Applied Mathematics and Mechanics*, *37*(11), 1467–1478. <https://doi.org/10.1007/s10483-016-2106-8>
- Harada, Y., Tsuchiya, F., Takeda, K., & Muneoka, T. (2009). Characteristics of ground freezing and thawing under snow cover based on long-term observation. *Seppyo*, *71*, 241–252.
- Hurrell, J. W., Holland, M. M., Gent, P. R., Ghan, S., Kay, J. E., Kushner, P. J., et al. (2013). The community Earth system model: A framework for collaborative research. *Bulletin of the American Meteorological Society*, *94*(9), 1339–1360. <https://doi.org/10.1175/BAMS-D-12-00121.1>
- Iwata, Y., Hayashi, M., Suzuki, S., Hirota, T., & Hasegawa, S. (2010). Effects of snow cover on soil freezing, water movement, and snowmelt infiltration: A paired plot experiment. *Water Resources Research*, *46*, W09504. <https://doi.org/10.1029/2009WR008070>
- Ji, P., Yuan, X., & Liang, X. Z. (2017). Do lateral flows matter for the hyperresolution land surface modeling? *Journal of Geophysical Research: Atmospheres*, *122*, 12,077–12,092. <https://doi.org/10.1002/2017JD027366>
- Jia, B., Xie, Z., Dai, A., Shi, C., & Chen, F. (2013). Evaluation of satellite and reanalysis products of downward surface solar radiation over East Asia: Spatial and seasonal variations. *Journal of Geophysical Research: Atmospheres*, *118*, 3431–3446. <https://doi.org/10.1002/jgrd.50353>
- Jumikis, A. R. (1978). Thermal geotechnics. *Soil Science*, *125*(6), 393. <https://doi.org/10.1097/00010694-197806000-00010>
- Lawrence, D. M., Oleson, K. W., Flanner, M. G., Thornton, P. E., Swenson, S. C., Lawrence, P. J., et al. (2011). Parameterization improvements and functional and structural advances in version 4 of the Community Land Model. *Journal of Advances in Modeling Earth Systems*, *3*, M03001. <https://doi.org/10.1029/2011MS000045>
- Li, X., Cheng, G., Jin, H., Kang, E., Che, T., Jin, R., et al. (2008). Cryospheric change in China. *Global and Planetary Change*, *62*(3–4), 210–218. <https://doi.org/10.1016/j.gloplacha.2008.02.001>
- Li, X., Cheng, G., Liu, S., Xiao, Q., Ma, M., Jin, R., et al. (2013). Heihe watershed allied telemetry experimental research (HiWATER): Scientific objectives and experimental design. *Bulletin of the American Meteorological Society*, *94*(8), 1145–1160. <https://doi.org/10.1175/BAMS-D-12-00154.1>
- Li, X., Lu, L., Cheng, G., & Xiao, H. (2001). Quantifying landscape structure of the Heihe River Basin, north-west China using FRAGSTATS. *Journal of Arid Environments*, *48*(4), 521–535. <https://doi.org/10.1006/jare.2000.0715>
- Liang, X., & Xie, Z. (2001). A new surface runoff parameterization with subgrid-scale soil heterogeneity for land surface models. *Advances in Water Resources*, *24*(9–10), 1173–1193. [https://doi.org/10.1016/S0309-1708\(01\)00032-X](https://doi.org/10.1016/S0309-1708(01)00032-X)
- Liang, X., & Xie, Z. (2003). Important factors in land–atmosphere interactions: Surface runoff generations and interactions between surface and groundwater. *Global and Planetary Change*, *38*(1–2), 101–114. [https://doi.org/10.1016/S0921-8181\(03\)00012-2](https://doi.org/10.1016/S0921-8181(03)00012-2)
- Lindsay, K., Bonan, G. B., Doney, S. C., Hoffman, F. M., Lawrence, D. M., Long, M. C., et al. (2014). Preindustrial-control and twentieth-century carbon cycle experiments with the Earth system model CESM1 (BGC). *Journal of Climate*, *27*(24), 8981–9005. <https://doi.org/10.1175/JCLI-D-12-00565.1>
- Liu, S., Xie, Z., & Zeng, Y. (2016). Discharge estimation for an ungauged inland river in an arid area related to anthropogenic activities: A case study of Heihe River Basin, northwestern China. *Advances in Meteorology*, *2016*, 1–11. <https://doi.org/10.1155/2016/6716501>
- Liu, S., Xu, Z., Wang, W., Jia, Z., Zhu, M., Bai, J., & Wang, J. (2011). A comparison of eddy-covariance and large aperture scintillometer measurements with respect to the energy balance closure problem. *Hydrology and Earth System Sciences*, *15*(4), 1291–1306. <https://doi.org/10.5194/hess-15-1291-2011>
- Maxwell, R. M., & Condon, L. E. (2016). Connections between groundwater flow and transpiration partitioning. *Science*, *353*(6297), 377–380. <https://doi.org/10.1126/science.aaf7891>
- Niu, G. Y., Yang, Z. L., Dickinson, R. E., & Gulden, L. E. (2005). A simple TOPMODEL-based runoff parameterization (SIMTOP) for use in global climate models. *Journal of Geophysical Research*, *110*, D21106. <https://doi.org/10.1029/2005JD006111>
- Oleson, K. (2013). Technical description of version 4.5 of the Community Land Model (CLM), Natl. Cent. for Atmos. Res., Tech. Note NCAR/TN-503+ STR.
- Pang, Q., Cheng, G., Li, S., & Zhang, W. (2009). Active layer thickness calculation over the Qinghai–Tibet Plateau. *Cold Regions Science and Technology*, *57*(1), 23–28. <https://doi.org/10.1016/j.coldregions.2009.01.005>
- Pokhrel, Y. N., Hanasaki, N., Wada, Y., & Kim, H. (2016). Recent progresses in incorporating human land–water management into global land surface models toward their integration into Earth system models. *Wiley Interdisciplinary Reviews: Water*, *3*(4), 548–574. <https://doi.org/10.1002/wat2.1150>
- Pokhrel, Y. N., Koirala, S., Yeh, P. J. F., Hanasaki, N., Longuevergne, L., Kanae, S., & Oki, T. (2015). Incorporation of groundwater pumping in a global land surface model with the representation of human impacts. *Water Resources Research*, *51*, 78–96. <https://doi.org/10.1002/2014WR015602>
- Ran, Y., Li, X., Lu, L., & Li, Z. (2012). Large-scale land cover mapping with the integration of multi-source information based on the Dempster–Shafer theory. *International Journal of Geographical Information Science*, *26*(1), 169–191. <https://doi.org/10.1080/13658816.2011.577745>
- Schuur, E. A., Vogel, J. G., Crummer, K. G., Lee, H., Sickman, J. O., & Osterkamp, T. (2009). The effect of permafrost thaw on old carbon release and net carbon exchange from tundra. *Nature*, *459*(7246), 556–559. <https://doi.org/10.1038/nature08031>
- Shah, T. (2014). Towards a managed aquifer recharge strategy for Gujarat, India: An economist's dialogue with hydro-geologists. *Journal of Hydrology*, *518*, 94–107. <https://doi.org/10.1016/j.jhydrol.2013.12.022>
- Shi, C., Xie, Z., Qian, H., Liang, M., & Yang, X. (2011). China land soil moisture EnKF data assimilation based on satellite remote sensing data. *Science China Earth Sciences*, *54*(9), 1430–1440. <https://doi.org/10.1007/s11430-010-4160-3>
- Siebert, C., Rödiger, T., Mallast, U., Gräbe, A., Guttman, J., Laronne, J. B., et al. (2014). Challenges to estimate surface-and groundwater flow in arid regions: The Dead Sea catchment. *Science of the Total Environment*, *485*, 828–841.
- Tian, Y., Zheng, Y., & Zheng, C. (2016). Development of a visualization tool for integrated surface water–groundwater modeling. *Computational Geosciences*, *86*, 1–14. <https://doi.org/10.1016/j.cageo.2015.09.019>
- Wada, Y., Wisser, D., Eisner, S., Flörke, M., Gerten, D., Haddeland, I., et al. (2013). Multimodel projections and uncertainties of irrigation water demand under climate change. *Geophysical Research Letters*, *40*, 4626–4632. <https://doi.org/10.1002/grl.50686>

- Wang, G., Li, Y., Wu, Q., & Wang, Y. (2006). Impacts of permafrost changes on alpine ecosystem in Qinghai-Tibet Plateau. *Science in China, Series D: Earth Sciences*, 49(11), 1156–1169. <https://doi.org/10.1007/s11430-006-1156-0>
- Wang, T. (2006). *1:4000000 map of the glaciers frozen ground and deserts in China*. Beijing: Science Press.
- Wood, E. F., Roundy, J. K., Troy, T. J., Van Beek, L., Bierkens, M. F., Blyth, E., et al. (2011). Hyperresolution global land surface modeling: Meeting a grand challenge for monitoring Earth's terrestrial water. *Water Resources Research*, 47, W05301. <https://doi.org/10.1029/2010WR010090>
- Wu, J., Ding, Y., Ye, B., Yang, Q., Zhang, X., & Wang, J. (2010). Spatio-temporal variation of stable isotopes in precipitation in the Heihe River Basin, northwestern China. *Environment and Earth Science*, 61(6), 1123–1134. <https://doi.org/10.1007/s12665-009-0432-7>
- Xia, J., McGuire, A. D., Lawrence, D., Burke, E., Chen, G., Chen, X., et al. (2017). Terrestrial ecosystem model performance in simulating productivity and its vulnerability to climate change in the northern permafrost region. *Journal of Geophysical Research: Biogeosciences*, 122, 430–446. <https://doi.org/10.1002/2016JG003384>
- Xie, C., & Gough, W. A. (2013). A simple thaw-freeze algorithm for a multi-layered soil using the Stefan equation. *Permafrost and Periglacial*, 24(3), 252–260.
- Xie, Z., Di, Z., Luo, Z., & Ma, Q. (2012). A quasi-three-dimensional variably saturated groundwater flow model for climate modeling. *Journal of Hydrometeorology*, 13(1), 27–46. <https://doi.org/10.1175/JHM-D-10-05019.1>
- Xie, Z., Wang, L., Jia, B., & Yuan, X. (2016). Measuring and modeling the impact of a severe drought on terrestrial ecosystem CO₂ and water fluxes in a subtropical forest. *Journal of Geophysical Research: Biogeosciences*, 121, 2576–2587. <https://doi.org/10.1002/2016JG003437>
- Xie, Z., Zeng, Y.-J., Xia, J., Qin, P.-H., Jia, B.-H., Zou, J., & Liu, S. (2017). Coupled modeling of land hydrology–regional climate including human carbon emission and water exploitation. *Advances in Climate Change Research*, 8(2), 68–79. <https://doi.org/10.1016/j.accre.2017.05.001>
- Xiong, Z., & Yan, X. (2013). Building a high-resolution regional climate model for the Heihe River Basin and simulating precipitation over this region. *Chinese Science Bulletin*, 58(36), 4670–4678. <https://doi.org/10.1007/s11434-013-5971-3>
- Yang, K., He, J., Tang, W., Qin, J., & Cheng, C. C. (2010). On downward shortwave and longwave radiations over high altitude regions: Observation and modeling in the Tibetan Plateau. *Agricultural and Forest Meteorology*, 150(1), 38–46. <https://doi.org/10.1016/j.agrformet.2009.08.004>
- Yao, Y., Zheng, C., Tian, Y., Liu, J., & Zheng, Y. (2015). Numerical modeling of regional groundwater flow in the Heihe River Basin, China: Advances and new insights. *Science China Earth Sciences*, 58(1), 3–15. <https://doi.org/10.1007/s11430-014-5033-y>
- Yi, S., Arain, M. A., & Woo, M. K. (2006). Modifications of a land surface scheme for improved simulation of ground freeze-thaw in northern environments. *Geophysical Research Letters*, 33, L13501. <https://doi.org/10.1029/2006GL026340>
- Yuan, X., Zhang, M., & Wang, L. (2017). Understanding and seasonal forecasting of hydrological drought in the anthropocene. *Hydrology and Earth System Sciences*, 21(11), 5477–5492. <https://doi.org/10.5194/hess-21-5477-2017>
- Zeng, Y., Xie, Z., & Liu, S. (2017). Seasonal effects of irrigation on land-atmosphere latent heat, sensible heat, and carbon fluxes in semiarid basin. *Earth System Dynamics*, 8(1), 113–127. <https://doi.org/10.5194/esd-8-113-2017>
- Zeng, Y., Xie, Z., Yu, Y., Liu, S., Wang, L., Jia, B., et al. (2016). Ecohydrological effects of stream–aquifer water interaction: A case study of the Heihe River basin, northwestern China. *Hydrology and Earth System Sciences*, 20(6), 2333–2352. <https://doi.org/10.5194/hess-20-2333-2016>
- Zeng, Y., Xie, Z., Yu, Y., Liu, S., Wang, L., Zou, J., et al. (2016). Effects of anthropogenic water regulation and groundwater lateral flow on land processes. *Journal of Advances in Modeling Earth Systems*, 8(3), 1106–1131. <https://doi.org/10.1002/2016MS000646>
- Zeng, Y., Xie, Z., & Zou, J. (2017). Hydrologic and climatic responses to global anthropogenic groundwater extraction. *Journal of Climate*, 30(1), 71–90. <https://doi.org/10.1175/JCLI-D-16-0209.1>
- Zhang, M., Wang, S., Fu, B., Gao, G., & Shen, Q. (2018). Ecological effects and potential risks of the water diversion project in the Heihe River Basin. *Science of the Total Environment*, 619, 794–803.
- Zhong, B., Yang, A., Nie, A., Yao, Y., Zhang, H., Wu, S., & Liu, Q. (2015). Finer resolution land-cover mapping using multiple classifiers and multisource remotely sensed data in the Heihe river basin. *IEEE Journal of Selected Topics in Applied Earth Observations and Remote Sensing*, 8(10), 4973–4992. <https://doi.org/10.1109/JSTARS.2015.2461453>
- Zhou, J., Hu, B. X., Cheng, G., Wang, G., & Li, X. (2011). Development of a three dimensional watershed modelling system for water cycle in the middle part of the Heihe rivershed, in the west of China. *Hydrological Processes*, 25(12), 1964–1978. <https://doi.org/10.1002/hyp.7952>
- Zou, J., Xie, Z., Yu, Y., Zhan, C., & Sun, Q. (2014). Climatic responses to anthropogenic groundwater exploitation: A case study of the Haihe River Basin, northern China. *Climate Dynamics*, 42(7–8), 2125–2145. <https://doi.org/10.1007/s00382-013-1995-2>
- Zou, J., Xie, Z., Zhan, C., Qin, P., Sun, Q., Jia, B., & Xia, J. (2015). Effects of anthropogenic groundwater exploitation on land surface processes: A case study of the Haihe River Basin, northern China. *Journal of Hydrology*, 524, 625–641. <https://doi.org/10.1016/j.jhydrol.2015.03.026>